Using a Förster-resonance energy transfer (FRET)-based detection system (FedEcs) to monitor nanoparticle cargo delivery to the brain

Igor Khalin[1,2,C], Nagappanpillai Adarsh[3,4], Martina Schifferer[5,6], Antonia Wehn[1,7], Valeria J. Boide-Trujillo[3], Uta Mamrak[1], Joshua Shrouder[1], Thomas Misgeld[5,6,8], Severin Filser[1,9,*], Andrey Klymchenko[3,*], Nikolaus Plesnila[1,6,*,C]

[1]*Institute for Stroke and Dementia Research (ISD), LMU University Hospital, LMU Munich, Germany*
[2]*Normandie University, UNICAEN, INSERM UMR-S U1237, Physiopathology and Imaging of Neurological Disorders (PhIND), GIP Cyceron, Institute Blood and Brain @ Caen-Normandie (BB@C), Caen, France*
[3]*Laboratory de Biophotonique et Pharmacologie, University of Strasbourg, Strasbourg, France*
[4]*Department of Polymer Chemistry, Government College Attingal, Thiruvananthapuram, Kerala, India*
[5]*German Center for Neurodegenerative Diseases (DZNE), Munich, Germany*
[6]*Munich Cluster of Systems Neurology (SyNergy), Munich, Germany*
[7]*University of Munich Medical Center, Department of Neurosurgery, Munich, Germany*
[8]*Institute of Neuronal Cell Biology, Technical University Munich, Munich, Germany*
[9]*Core Research Facilities and Services-Light Microscope Facility, German Center for Neurodegenerative Diseases (DZNE), Bonn, Germany.*

* - equally contributed

[C] – corresponding authors; igor.khalin@inserm.fr; Nikolaus.Plesnila@med.uni-muenchen.de

Abstract

Nanotechnology holds great promise to improve delivery of therapeutics to the brain. Current experimental approaches are, however, hampered by the lack of tools to dynamically monitor cargo delivery *in vivo*. We developed highly fluorescent lipid nanodroplets (LNDs) that carry a Förster-resonance energy transfer (FRET)-based drug delivery detection system able to monitor cargo release (FedEcs) *in vivo*. We investigated the distribution, stability, and cargo release of FedEcs-LNDs in the healthy and ischemic mouse brain by intravital multiphoton microscopy. We dynamically observed that LNDs accumulated within cerebral microclots after ischemia, caused by magnetic nanoparticles (Nano-stroke), and released their cargo. Furthermore, the blood-brain barrier (BBB) became permeable at sites of microclots thereby allowing FedEcs-LNDs to cross the BBB and to deliver their cargo to the brain parenchyma. Consequently, FedEcs represents a novel tool to quantitatively investigate the nanocarriers biodistribution and cargo release using intravital microscopy and may thus tremendously ease their translational validation.

Key words: nanocarrier; FRET; stroke; microthrombi; blood-brain barrier;

38 **Introduction**

39 Nanotechnology is currently revolutionizing the delivery of therapeutics, however, nanomedicines
40 for the treatment of brain diseases are sparse. Among existing nanoscale platforms, lipid nanodroplets
41 (LNDs) hold particular promise[1]. LNDs have a lipid membrane and a liquid core thereby mimicking low-
42 dense lipoproteins. Their liquid core is an attractive reservoir for encapsulation of drugs and contrast
43 agents[1] and their lipid shell is biocompatible and therefore generally recognized as safe (GRAS) for the
44 application in patients[2-4]. LNDs are characterized by a long circulation time in blood, which make them
45 attractive for targeting tissues[5]. In particular, previous studies showed that LNDs remained intact in
46 the blood circulation for multiple hours after injection and accumulated in tumours in nearly intact
47 form[5].

48 Despite these advantageous properties, investigating the biodistribution of LNDs and other NPs in
49 the brain remains a fundamental challenge because current detection modalities are not well suited
50 to detect whether NPs cross the blood-brain barrier (BBB), enter the brain parenchyma, and release
51 their cargo. To overcome this issue, we developed highly fluorescent LNDs which are detectable *in vivo*
52 and carry a Förster-resonance energy transfer (FRET)-based drug delivery detection system (FedEcs)
53 which allows the visualization of cargo release *in vivo*. Using *in vivo* 2-photon microscopy, correlative
54 light-electron microscopy, and a mouse model of cerebral ischemia based on magnetic nanoparticles
55 (Nano-stroke), we observed that 30 nm FedEcs-LNDs accumulate in microthrombi forming in brain
56 capillaries after a stroke, cross the BBB, and release their cargo at both microthrombi and brain.

57 **Results**

58 **Development of highly fluorescent lipid nanodroplets (LNDs) carrying a Förster-resonance energy**
59 **transfer (FRET)-based cargo delivery detection system (FedEcs)**

60 We sought to design a highly fluorescent nanodroplets which harnesses FRET to dynamically assess
61 the structural integrity of the particles and the release of their encapsulated cargo. To that end, we
62 formulated LNDs from LabrafacWL and Cremophor ELP® by a spontaneous nanoemulsification[6] and
63 loaded them with two fluorophores which undergo FRET. The fluorescent dye F888, which was
64 specially designed for high loading into LNDs and high fluorescence intensity following 2-photon
65 excitation[7], was selected as FRET donor and the Cy3 derivative DiI was selected as FRET acceptor. DiI
66 was coupled to tetraphenylborate (TPB) to ensure efficient encapsulation inside LNDs with minimal
67 dye leakage[8] (**Figure 1A; Suppl. Figure S1 A**). Upon degradation of the LNDs and/or cargo release, the
68 distance between the donor and acceptor dyes increases thereby leading to the loss of FRET and a
69 subsequent reduction of the ratio between donor and acceptor fluorescence intensity (**Figure 1B**)[5].
70 This property of the LNDs should now function as a FRET-based cargo delivery detection system
71 (FedEcs). In contrast to previously reported FRET-LNDs operating in NIR region for whole mice

imaging[5], here we propose FRET-LNDs specially designed for 2-photon intravital imaging in capillary

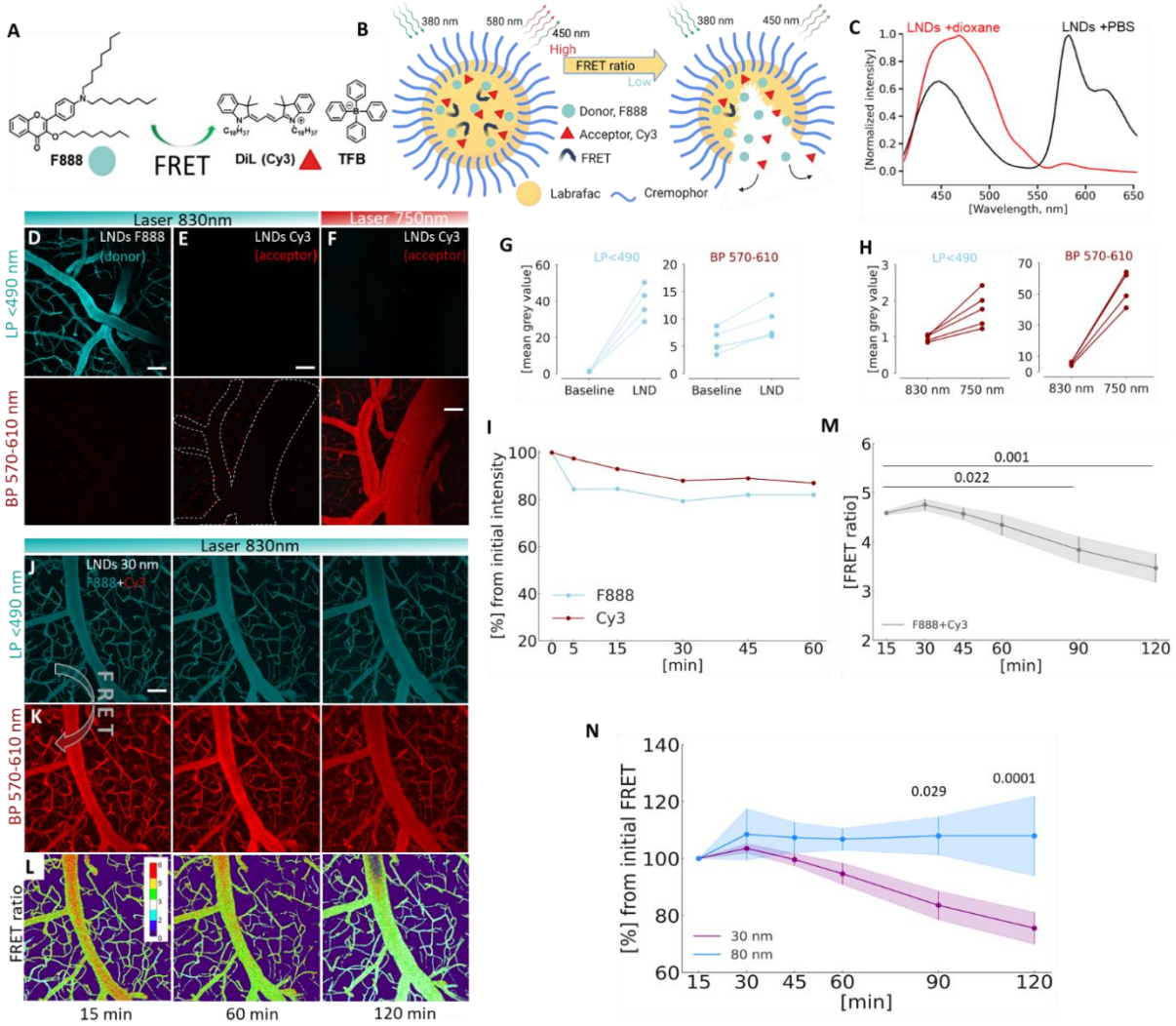

Figure 1. LNDs loaded with FRET system enable real-time *in vivo* quantitative fluorescent ratiometric imaging of nanocarrier (NC) integrity. A. Chemical structure of F888 and DiI (Cy3) coupled with a counterion tetraphenylborate, which causes FRET. Experiment design. **B.** Concept of FRET NCs that can shift their colour upon carrier decomposition, thus reducing the total FRET ratio. Schematic drawing of a LND consisting of an oil core (yellow; Labrafac WL), surfactant (blue; Cremaphore, Kolliphor® ELP), and the fluorescent FRET pair dyes F888 (blue shere) and Cy3 (red triangle) bound to a hydrophobic counter-ion. **C.** Fluorescence spectrum of FRET FRET-LNDs containing F888 and DiI-TPB (2 wt% loading each) diluted in PBS (back) and dioxane (red). **D-F.** Representative 2-photon images of mouse cortical vessels after injection of 30-nm LNDs loaded solely by F888 (donor) and Cy3 (acceptor). Maximum intensity projection (MIP) of 150 µm Z-stacks; laser power 4.5-13%; donor channel – LP<490 nm; acceptor channel – BP 570-610 nm; scale bar - 50 µm. **D.** Injected 30-nm LNDs loaded with F888 (donor), excitation laser wavelength 830 nm. Presence of bright fluorescent signal in donor channel. **E.** Injected 30-nm LNDs loaded with Cy3 (acceptor), excitation laser wavelength 830 nm. Absence of a signal in both the donor and acceptor channel. Dashed line outlines invisible vessel, which become visible only in 750 nm. **F.** Injected 30-nm LNDs loaded with Cy3 (acceptor), excitation laser wavelength switched to 750 nm. Presence of bright fluorescent signal in acceptor channel. **G.** Increase in fluorescent intensity after injection of donor-loaded LNDs (n=5 regions of interest in the vessels) in the donor (LP<490) and acceptor (BP 570-610 nm) channel. **H.** Shifting of the laser wavelength from 830 nm to 750 nm increases fluorescent intensity of the acceptor-loaded LNDs (n=5 regions of interest in the vessels) in both the donor and acceptor channel. **I.** Stability of LNDs loaded by F888 (donor) and Cy3 (acceptor) in the cerebral microcirculation of naïve mice during 1 hour (n=1). **J, K.** Representative 2-photon MIP images of mouse cortical vessels 15-120 min after injection of 30-nm FedEcs-LNDs loaded by FRET pair (F888+Cy3), excitation laser wavelength 830 nm. Due to the FRET effect, the acceptor become visible by BP 570-610 detector under a laser wavelength of 830 nm. **L.** By colour coding the ratiometric changes of the FRET ratio, it enables us to perform direct 3D real-time imaging of NC integrity in the blood

circulation. **M.** Quantification of time-depended LNDs disintegration in the mouse brain vasculature using FRET ratio. Data are presented as mean ± standard deviation (SD). One-way ANOVA was used, n=3. **N.** Comparative analysis of the degradation of circulated LNDs of two different sizes (30-nm (from M.) and 80-nm) using FRET ratio. Data presented as mean ± SD. Two-way ANOVA was used, n=3.

resolution. LNDs with diameter 30- and 80-nm, containing either the donor, acceptor, or both dyes were formulated (**Suppl. Figure S1B**). At an excitation wavelength of 380 nm, LNDs of both sizes showed the fluorescent properties of the donor, *i.e.* fluorescence emission at 450 nm, as well as a second fluorescence peak at 580 nm, corresponding to the expected emission of the acceptor due to FRET (**Suppl. Figure S1 C,D**). The LNDs generated are composed 98% of lipids and 2% of their constitution is represented by the donor and acceptor fluorophores respectively. At this weight, FRET efficiency between the donor and acceptor reached 86% for 30 and 80 nm LNDs (**Suppl. Figure S1 E**). Dilution of FedEcs-LNDs into dioxane, which is expected to destroy LNDs, led to the loss of the FRET signal, so that the emission was dominated by the donor emission (**Figure 1C**). These data demonstrate that the currently developed FRET system can detect LND integrity/cargo delivery.

Using FedEcs to investigate the stability of LNDs in healthy blood vessels *in vivo*

To investigate the critical issue of whether FedEcs-LNDs are bright enough to be visualized *in vivo* and to validate their functionality, we injected FedEcs-LNDs systemically into mice and investigated the cerebral vasculature by *in vivo* 2-photon microscopy (2-PM). FedEcs-LNDs were bright enough to be visualized *in vivo* and LNDs containing either the donor (F888) or acceptor (Dil-TPB) behaved as expected, *i.e.* fluorescence was only observed when the particles were excited with the wavelength specific for the respective fluorophore (830 or 750 nm; **Figure 1D-H**). Longitudinal imaging confirmed these results suggesting that LNDs loaded with both fluorophores are stable *in vivo* (**Figure 1I**). LNDs loaded with FRET donors and acceptors (FedEcs-LNDs) emitted bright fluorescence in both channels (**Figure 1J, K**), suggesting that FRET occurs and can be dynamically assessed in vivo. Thereby, we can dynamically assess real-time particle integrity using the FRET ratio, quantifying the acceptor/donor ratio (**Figure 1L**). Longitudinal analysis of the FRET ratio of circulating 30-nm LNDs in healthy mice showed a slow decrease in the FRET signal, which reached 80% of the initial FRET ratio value over 120 min (**Figure 1M**). 80-nm LNDs had a substantially higher (p=0.0001) stability in the blood circulation since they remained intact for two hours (**Figure 1N**) most likely due to a higher oil to surfactant ratio. Thereby, we can dynamically assess real-time particle integrity using the FRET ratio, quantifying the acceptor to donor ratio. To our knowledge, this is the first report of a nanoparticle system able to produce a stable FRET signal *in vivo* suitable to intravital 2-PM.

133 **Employing FedEcs to define the distribution of LNDs after ischemic stroke *in vivo***

134 To investigate how LNDs behave under pathological conditions, we induced focal cerebral
135 ischemia by occluding the middle cerebral artery of a mouse with an endovascular filament for one
136 hour and systemically injected highly fluorescent LNDs 30 min after reperfusion (**Suppl. Figure S2A-B**).
137 We focused on 30 nm LNDs, because we recently showed that NPs of this size are small enough to
138 cross the blood-brain barrier via transcytosis[9]. Animals were sacrificed 60 minutes after LND injection
139 and we detected a wide spread accumulation of LNDs within the ischemic territory by histological
140 analysis (**Suppl. Figure S2C**). Staining of blood vessels (lectin) and red blood cells (Ter119) indicated
141 that LNDs were located within cerebral vessels and colocalized with trapped red blood cells indicative
142 of thrombus formation. A high intensity area around LND-stained vessel occlusions suggested that
143 LNDs may have extravasated into the brain parenchyma (**Suppl. Figure S2C, i-iii**).

144 We then aimed to investigate this process dynamically and with the highest possible resolution
145 to decipher the mechanism by which LNDs crossed the blood brain barrier and whether the
146 accumulation of LNDs in ischemic brain may have affected their ability to carry and deliver cargo. For
147 this purpose, we developed a novel stroke model based on a technique previously used to induce focal
148 cerebral ischemia in juvenile mice[10]. This particular model uses magnetic nanoparticles (MNP) to
149 transiently occlude cortical blood vessels. In detail, animals received a systemic injection of MNP and
150 subsequently a strong mini-magnet was placed on top of the cranial window implanted for *in vivo*
151 imaging (**Suppl. Figure S3A**). The magnetic field trapped the 200 nm pegylated MNPs within the
152 cerebral vasculature (**Suppl. Figure S3B i-ii**) thereby causing cerebral ischemia (Nano-Stroke).
153 Reperfusion was induced by removing the magnet after one hour (**Suppl. Figure S3B iii-iv**). This model
154 occluded cortical blood vessels up to a depth of 500 µm (**Suppl. Figure 3C-E**) and allowed immediate
155 live 2-PM of reperfused cerebral vessels (**Suppl. Figure S3F**) followed by histological evaluation (**Suppl.
156 Figure S3G-K**). Using the Nano-Stroke model and FedEcs-LNDs we investigated the biodistribution of
157 systemically applied LNDs after experimental stroke by *in vivo* 2-PM (**Figure 2A**). First, we focused on
158 LNDs with preserved integrity according to their FRET (acceptor) signal (**Figure 2B**). Post-reperfusion,
159 we observed LND accumulation within non-flowing segments of cerebral vessels (**Figure 2C, yellow
160 arrow**). Some LND accumulations **(Figure 2D, yellow arrow)** were accompanied by subsequent
161 extravasation of LNDs into the brain parenchyma (**Figure 2D**, **80 min, red arrow**). Quantification
162 showed that the number of LND accumulations 80 min after ischemic stroke was 8-fold higher than in
163 sham operated mice **(Figure 2E;** $p<0.0001$**; Ext. data Fig. S4)** and that 90% of all observed micro-
164 occlusions occurred in vessels less than 6 µm, *i.e*. brain capillaries (**Figure 2F**), implying that LNDs were
165 trapped in microvascular-occlusions. Interestingly, 25% of all microthrombi observed after stroke were
166 associated with extravasation of LNDs **(Figure 2G)**, while no extravasations were detected in sham
167 operated animals. Most importantly, extravasation of LNDs were only observed at sites where micro-

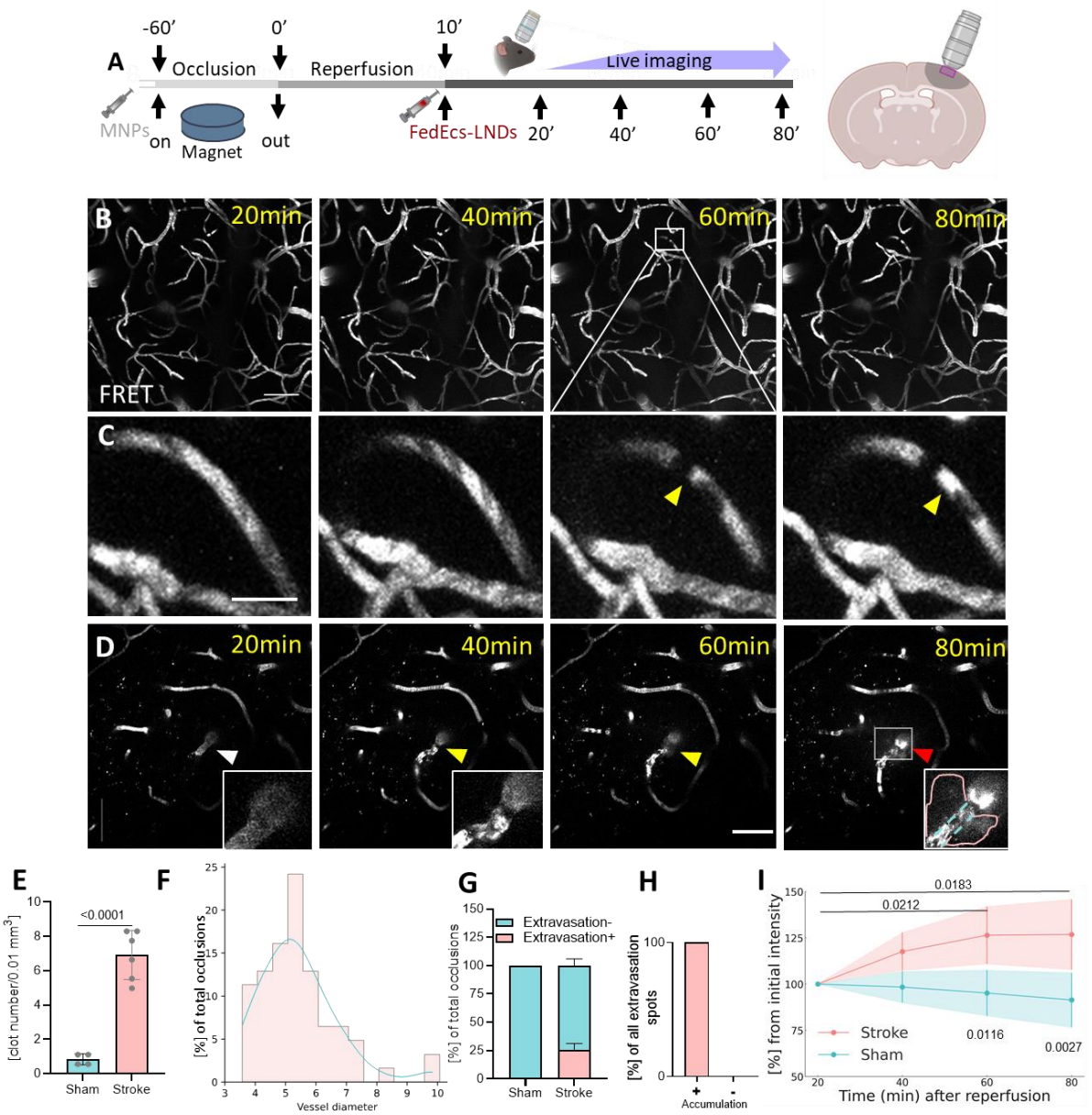

Figure 2. Spontaneous capillary microclot formation following Nano-stroke opens the blood-brain barrier for FedEcs-LNDs. A. Experiment design as described at **Suppl. Fig. S3A** with additional longitudinal intravital imaging every 20 minutes during 1 hour. Schematic representation of the field of view during intravital microscopy. Grey zone – the area under magnet with 60-min-occluded vessels. Magenta – imaging area (depth is ~150 µm). **B.** A representative maximum intensity projection (MIP) of Z-stack of longitudinal 2-photon intravital imaging of cortical area after Nano-stroke model in mouse injected with FedEcs lipid nanodroplets (LNDs). Scale bar – 50 µm. **C.** Zoomed from 4B, representative images of spontaneous microvascular clot formation with subsequently accumulated LNDs (yellow arrow). Scale bar – 10 µm. **D.** Representative longitudinal real-time images of spontaneous microvascular clot formation followed by extravasation of LNDs into the brain parenchyma (yellow arrow). Scale bar - 50 µm. **E.** Analysis of numbers of microvascular clots at 80 min post-reperfusion compared to sham animals. Data are presented as mean ± standard deviation (SD). Unpaired t-test. Stroke: N=79 clots (6 mice); Sham – 4 mice. **F.** Size-distribution of the vessels with microclots. Data are presented as proportion of vessel diameter where microclots were detected. N=62 clots (6 mice). **G.** Proportion of microvascular clots associated with extravasation of the LNDs. Data represented as mean ± SD. N=4 (sham) and n=6 (nano-stroke). **H.** Analysis of association between microclot (accumulation) and blood-brain barrier dysfunction (extravasation). N=20. **I.** Longitudinal analysis of the accumulation of FedEcs LNDs in the ischemic brain area. Data represented as mean ± SD. Two-way ANOVA was used, n=4 (sham) and n=6 (Nano-stroke).

186 occlusions formed **(Figure 2H)**, suggesting that micro-occlusions compromised the permeability of the
187 adjacent capillary wall and were critically involved in the opening of the BBB. Longitudinal *in vivo*
188 imaging of LNDs allowed us to detect that particles gradually accumulated within the ischemic brain
189 parenchyma (**Figure 2I**). Altogether, LNDs do not only accumulate within the vessel lumen after
190 ischemic stroke, but also extravasate into the ischemic brain parenchyma. Thus, our data visualize for
191 the first time that LNDs enter the ischemic brain and may thus have the potential to carry drugs into
192 ischemic tissue.

193 Since MNPs are visible at bright-field microscope, photoluminescent under 2-photon
194 excitation, as well as electron-dense, they can be used as fiducial markers for correlative light-electron
195 microscopy (CLEM). Capitalizing on this feature we monitored LNDs accumulations and extravasation
196 *in vivo* and subsequently relocated these "hot-spots" in serial electron microscopy based on the
197 retained MNPs inside the occluded blood vessel **(Suppl. Figure S5; Methods**). This allowed us to match
198 images obtained by 2-PM *in vivo* with the ultrastructural reconstructions derived from serial electron
199 micrgraphs obtained by scanning electron microscopy (SEM). For this purpose, we induced MNPs-
200 mediated cerebral ischemia in mice for one hour, injected FedEcs-LNDs 20 min after reperfusion, and
201 imaged cerebral microvessels by *in vivo* 2-PM **(Figure 3A)**. We identified three micro-occlusions by *in*
202 *vivo* microscopy: two without extravasation, which appeared at different time points – 20 min and 80
203 min after reperfusion **(Figure 3B, yellow and magenta arrows)** and one with extravasations **(Figure 3C,**
204 **grey arrow)** and re-identified them by CLEM **(Figure 3D; Movie S01)**. After reconstructing both vessel
205 segments in 3D (**Figure 3E, F**; **Movie S02, 03**), we identified the cellular composition and the
206 microstructure of the occluded vessels (**Figure 3E-I**). Microglial and pericytes surrounded the occluded
207 vessels, while erythrocytes, platelets and LNDs co-localized within the occlusions (**Figure 3E-F**). When
208 further zooming in into the ultrastructure of the microvascular occlusions, we found fibrin nets (orange
209 arrow) in between red blood cells, further suggesting that the observed occlusions were microthrombi
210 (**Figure 3G and H**). Collectively, these findings show that Nano-Stroke technique induces bona fide
211 microclots, in and around which LNDs are trapped, independently of whether the clots formed early
212 or late after the beginning of the reperfusion period.

213 Using CLEM, we precisely investigated the microstructure of brain endothelial cells (BECs) in
214 the proximity of microclots (**Figure 3Gii-iii & Hii-iii**). Interestingly, microclots which formed early after
215 reperfusion according to *in vivo* imaging contained erythrocytes of altered morphology, while those
216 clots that formed later had erythrocytes with the normal biconcave shape (**Figure 3Gii&Hii**). The BECs
217 in the vicinity of older clots had a much higher number of caveolae (23 caveolae/µm; **Figure 3Giii**) than
218 BECs next to fresh microclots (2.8 caveolae/µm; **Figure 3Hii,iii**), implicating that a persisting contact
219 between BECs and clots, which lead to lack of oxygen, may induce the formation of caveolae, the
220 prerequisite for the subsequent extravasation of LNDs into the brain parenchyma. This conclusion is

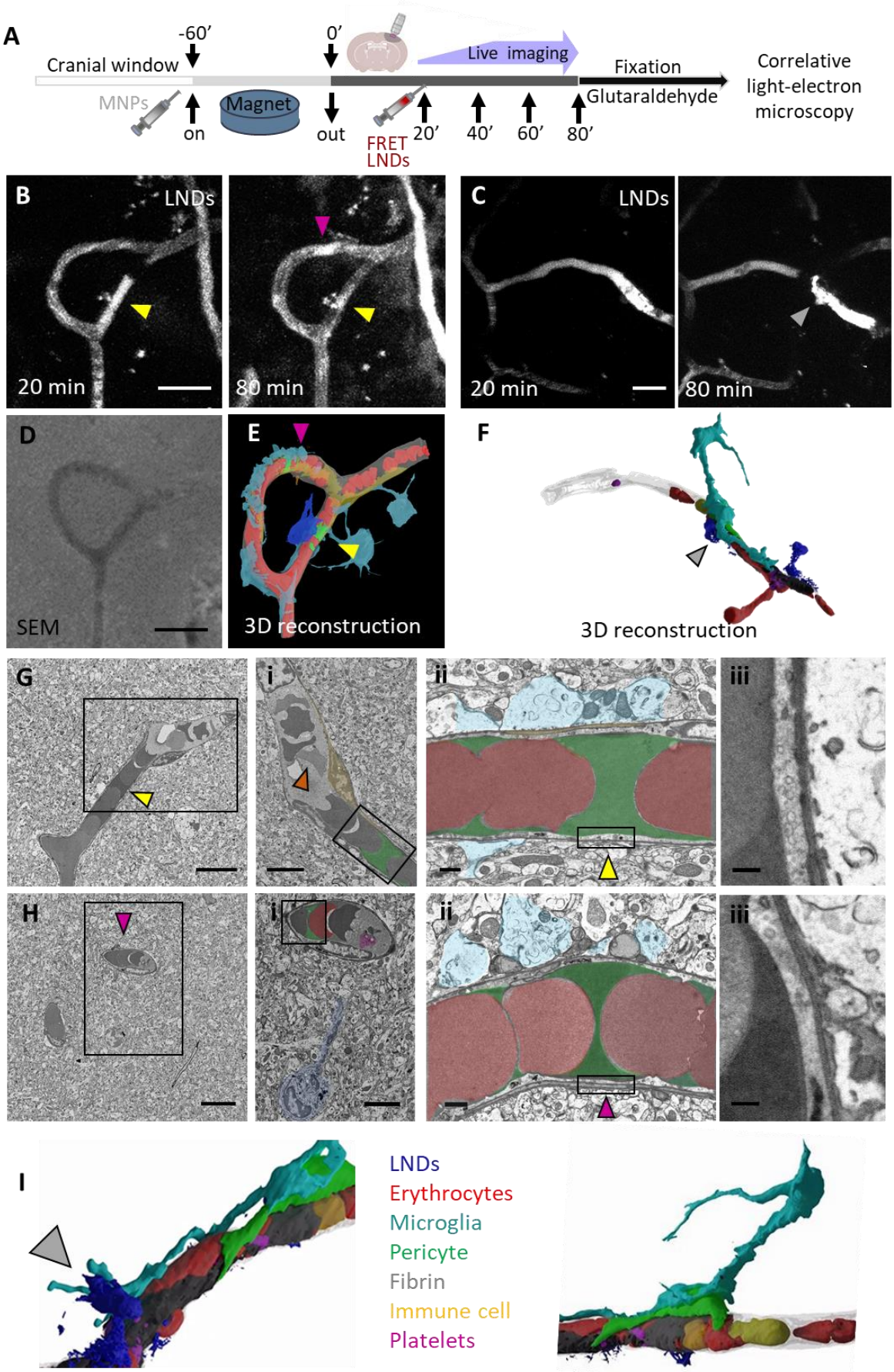
A
-60′
0′
Cranial window
Live imaging
Fixation
Glutaraldehyde
Correlative light-electron microscopy
MNPs
on
Magnet
out
FRET LNDs
20′
40′
60′
80′
B
LNDs
20 min
80 min
C
LNDs
20 min
80 min
D
SEM
E
3D reconstruction
F
3D reconstruction
G
i
ii
iii
H
i
ii
iii
I
LNDs
Erythrocytes
Microglia
Pericyte
Fibrin
Immune cell
Platelets

Figure 3. Correlative light-electron microscopy revealed ultrastructural changes in sites of accumulation and extravasation of FedEcs-LNDs. A. Experiment design as described in **Suppl. Fig. S3A** with longitudinal intravital imaging during 60 minutes followed by fixation, embedding and serial sectioning for correlated volume electron microscopy (EM) by automated serial sections to tape (ATUM; **Suppl. Fig. S5**). **B.** Representative 2-PM images of post-stroke mouse brain capillaries containing "old" (20 min post-reperfusion; yellow arrow) and "fresh" (80 min; magenta arrow) spontaneous microvascular clots. Scale bar 20 µm. **C.** Representative example of a microvascular clot (20 min) transitioning towards LNDs extravasation (80 min; grey arrow) into the brain parenchyma ("leaky" microclot). Scale bar 20 µm. **D.** Summed slices of a **s**canning electron microscopy (SEM) stack of the relocated region from the 2-PM experiment **(Suppl. Fig.S5)**. Scale bar 20 µm. **E.** Rendered three-dimensional reconstruction of the volume SEM data thereof. Red (erythrocytes); yellow (pericytes); green (LNDs); sky blue (astrocytes); dark blue (microglia); magenta (platelet). **F.** Rendered three-dimensional reconstruction of volume electron microscopy of the relocated region from **Fig. 3C**. Red – erythrocytes; dark blue – LNDs; cyan – microglia; grey – fibrin; green – pericyte; magenta – platelets; yellow – leukocytes; transparent grey – BEC. See in Movie S03. **G.-H.** Single, segmented high-resolution SEM images of the "old" (G; yellow arrow) and "fresh" (H; magenta arrow) microclots from 3B. Scale bar 10 µm. **G,i.** Zoomed area from G. containing an "old" microclot with accumulated LNDs (green) and a pericyte constricting the capillary (yellow). Orange arrow – dysmorphic erythrocytes trapped into fibrine. **G,ii.** Zoomed area from E,i containing an occluded capillary with accumulated LNDs (green) between erythrocytes (red). Sky blue – astrocytic endfeet. Yellow arrow – relocated capillary area with accumulated LNDs showing a higher than in normal capillaries fluorescent intensity in 2-PM. Scale bar – 1 µm. **G,iii.** Zoomed brain endothelium cell (BEC) from J,ii. containing a large amount of vesicular-like structures. Scale bar – 200 nm. **H,i.** Zoomed area from H. containing a "fresh" microclot with accumulated LNDs (green) between erythrocytes (red) and microglia cell (dark blue) with its processes directed towards the platelet cells (magenta) trapped into fibrine. **H,ii.** Zoomed area from H,i containing an occluded capillary with accumulated LNDs (green) between erythrocytes (red). Sky blue – astrocyte endfeet. Magenta arrow – relocated capillary area with accumulated LNDs having higher fluorescent intensity in 2-PM. Scale bar – 1 µm. **F,iii.** Zoomed BEC from F,ii. with low level of vesicular-like structures. Scale bar – 200 nm. **H,iii.** Zoomed BEC from H,ii. with high level of vesicular-like structures. Scale bar – 200 nm. **I.** Zoomed F. demonstrating that extravasation occurs from the place where microthrombi were formed. FedEcs LNDs – dark blue; Erythrocytes – red; Microglia – cyan; Pericyte – green; Fibrin – grey; Immune cell – yellow; Platelets – magenta. Grey arrow – place of extravasation relocated from **Fig. 3C**.

supported by the observation that LNDs indeed extravasate next to microclots (**Figure 3I, grey arrow**). Thus, our electron microscopy data show that stroke-induced persisting microclots within the cerebral microcirculation progressively promote endothelial transcytosis through caveolae, which may be associated with BBB opening and may therefore allow LNDs to enter the brain parenchyma.

To investigate this process on the functional level *in vivo*, mice received a systemic injection of LNDs and were then subjected to 60 min Nano-stroke. We then imaged the cerebral microcirculation by *in vivo* 2-PM before and after ischemia **(Suppl. Figure 6)**. Images obtained immediately after reperfusion showed multiple microclots co-localising with LND extravasation **(Suppl. Figure 6, yellow arrows)**, supporting our histological and EM findings that microclots serve as an entry point for LNDs into the brain parenchyma, *i.e.* occluding vessels by MNP locally opens the BBB.

Monitoring cargo delivery of LNDs in the brain using FedEcs

Entry of LNDs into the brain parenchyma is, however, not equivalent with cargo delivery. Therefore, we used the newly developed FedEcs functionality of our highly fluorescent LNDs to monitor whether LNDs decompose after being trapped in microclots and transmigrate into the brain

267 parenchyma. For this purpose, we measured the FRET ratio in flowing versus non-flowing segments of
268 the microvasculature after cerebral ischemia over-time by quantitative *in vivo* FRET imaging **(Figure**
269 **4A)**. We identified stable FRET ratios of LNDs circulating in plasma (**Figure 4B**, yellow colour), while the

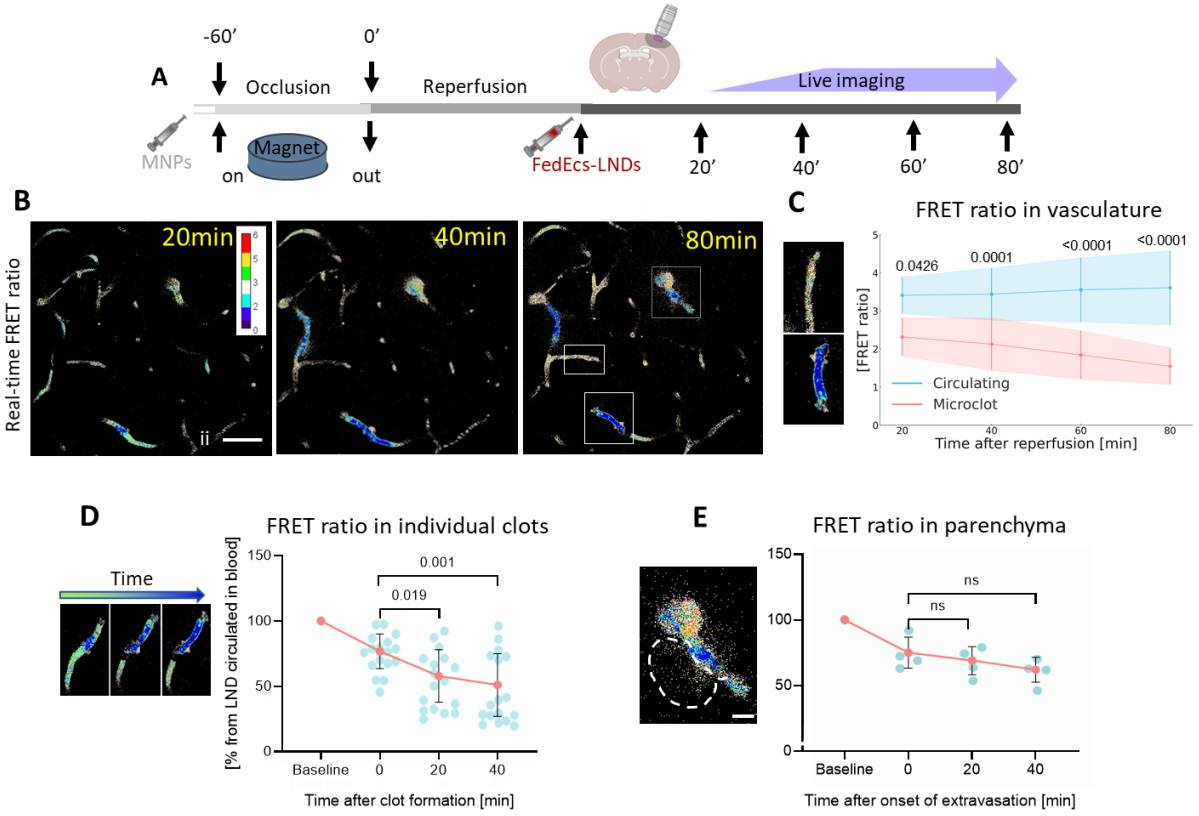

270

271 **Figure 4. FRET ratio reveals higher decomposition of FedEcs-LNDs in microclots, but not in brain parenchyma**
272 **as well as delivery of cargo into the brain parenchyma. A.** Experiment design. **B.** Representative longitudinal
273 real-time images of visualisation of FRET ratio related to decomposition of FedEcs-LNDs in vasculature of ischemic
274 brain area. Scale bar - 50 µm. **C.** Longitudinal analysis FRET ratio related to decomposition of FedEcs-LNDs in
275 vasculature of ischemic brain area during 80 minutes after recanalization. Data are presented as mean ± SD. Two-
276 way ANOVA was used, circulated n=16-17 ROIs; microclots n=6-13; 5 mice. **D.** Time-dependent analysis of relative
277 FRET changes of LNDs located inside individual clot. **E.** Time-dependent analysis of relative FRET changes of
278 extravasated into brain parenchyma LNDs. Data are presented as single points and mean ± SD. One-way ANOVA
279 was used, n= 17 clots and n=4 extravasations, respectively. Scale bar – 10 µm. Yellow arrow – clot; dashed area
280 – extravasated FedEcs-LNDs emitting FRET.
281

282 FRET ratio of LNDs trapped within microclots was significantly reduced (**Figure 4B**, blue colour). The
283 loss of FRET is caused by a loss of interaction between the two fluorophores undergoing FRET and is
284 therefore a quantitative measure of particle decomposition. From the first imaging time-point after
285 nano-stroke, clots could be visualized as non-flowing segments of the microcirculation. From on-set
286 these non-flowing segments had significantly lower FRET ratio than flowing segments, implying LNDs
287 in non-flowing segments behaved differently **(Figure 4C)**. Hence, our data indicate that LNDs are stable
288 in plasma, but start decomposing once being trapped in microclots. This observation is further
289 supported by the analysis of individual microclots over time (**Figure 4D**). Once trapped in a microclot,
290 the FRET ratio of LNDs starts declining and reaches about 50% of its baseline value after 40 min. These

291 data imply that non-flowing segments associated with micro-thrombi elicit LND degradation. Next, we
292 compared intravascular FRET ratio of LNDs with the FRET ratio of parenchymal LNDs that traversed the
293 BBB at the site of clots (roughly occurring in 25% of cases as was shown at **Figure 3G**). We could
294 selectively observe FRET signal from extravasated LNDs **(Figure 4E**, **dashed line)**, explicitly proving that
295 intact LNDs cross the BBB. Additionally, we found that the FRET ratio in parenchyma also decreases,
296 implying a slow degradation of LNDs overtime, but was insignificant **(Figure 4E)**. These findings may
297 suggest that the microenvironment of clots results in a faster decomposition of LNDs than the one
298 present in the brain parenchyma and that turbulence and shear stress at the site of freshly formed and
299 persistent clots results in the degradation of LNDs and a decrease in the FRET ratio over-time,
300 suggesting the cargo delivery system can harness the passive targeting of no-reflow after stroke and
301 exert a slow release of the intended cargo once LNDs have extravasated beyond the vasculature.

302 In summary, using highly fluorescent LNDs and FedEcs, a novel *in vivo* real-time cargo release
303 detection system, we assessed the biodistribution of nanoparticles-based drug carriers *in vivo* and
304 found that lipid nanodroplets accumulate inside microthrombi, cross the BBB, and enter the brain
305 parenchyma while releasing their cargo. Thus, FedEcs represents a novel and useful tool to investigate
306 the therapeutic potential of nanoparticle-based drug delivery systems and to directly visualize cargo
307 delivery *in vivo* with a high spatial and temporal resolution.

308 **Discussion**

309 Targeted drug delivery using nanotechnology has two conflicting aims: nanoparticles must
310 reliably enclose their cargo and transport it to the target tissue, but release it there effectively[11]. Both
311 aims are hard to achieve and even more challenging to investigate experimentally due to insufficient
312 technologies for particle tracking and cargo release in living organisms. In the current study we
313 developed highly fluorescent LNDs with a built-in cargo release signal based on FRET and used these
314 nanoparticles (NPs) to investigate the biodistribution of LNDs and cargo release in a novel, magnetic
315 NPs-based model of ischemic stroke in mice. Using *ex vivo* and *in vivo* multiphoton fluorescent
316 microscopy, we demonstrate that LNDs accumulate and thereby reliably label microthrombus
317 formation within the cerebral microcirculation after ischemic stroke. Microthrombi open the blood-
318 brain barrier (BBB) thereby enabling LNDs to extravasate into the brain parenchyma. *In vivo* FRET
319 imaging suggests that LNDs release their cargo within microthrombi and, at a lower rate, also in the
320 brain parenchyma. These data explain the cellular and subcellular mechanisms responsible for the
321 retention of liposomes in ischemic brain published earlier[12-14], define the exact site of particle
322 retention, and suggest LNDs as potential drug carriers for the delivery of therapeutics to the brain
323 under conditions where microthrombi are present, *i.e.* ischemic stroke or traumatic brain injury[9].

324 To investigate the biodistribution of systemically applied NPs in the brain after stroke, we had
325 to develop and improve several novel technologies. After observing retention of LNDs inside microclots

326 in the ischemic brain by confocal microscopy, we used *in vivo* 2-photon imaging to understand the
327 dynamics and the mechanism of this process. For this purpose, we developed a new MNPs-based
328 stroke model, Nano-Stroke, which allowed us to image exactly the same cerebral vessels before and
329 after reperfusion. The Nano Stroke model is based on the recently published SIMPLE stroke model
330 performed in pups[10]. We adapted the SIMPLE model to adult animals by implanting a chronic cranial
331 window, thus allowing us to visualize cerebral vessels in the ischemic brain longitudinally and with high
332 resolution. Combining the Nano-Stroke model with highly fluorescent, super-bright FedEcs-LNDs and
333 intravital 2-PM, we were able to demonstrate for the first time *in vivo* and in real-time that following
334 reperfusion systemically injected LNDs accumulate inside microthrombi and extravasate there, a so far
335 missed phenomenon due to the use of low-fluorescence NPs.

336 Accumulation of LNDs inside microclots after cerebral ischemia may have a large medical
337 potential. The standard treatment for ischemic stroke is recanalizing large cerebral arteries either by
338 dissolving or removing the occluding thrombus by systemic administration of recombinant tissue
339 plasminogen activator or by mechanical thrombectomy, respectively[15]. However, in many cases
340 recanalization of large cerebral vessels does not result in reperfusion of the cerebral microcirculation
341 and restoration of cerebral blood flow and may thus allow additional tissue damage to occur[16]. In
342 previous attempts to dissolve microthrombi after stroke researchers attached the main thrombus-
343 attaching protein (Cys-Arg-Glu-Lys-Ala) CREKA on the surface of nanocarrier[17-19], however, due to the
344 lack of appropriate imaging techniques it remained elusive whether these particles delivered their
345 cargo into microclots. In the current study, we did not use any active targeting strategy, still our LNDs
346 ended up in large numbers within microclots. This finding is per se interesting, since future approaches
347 to target microthrombi may include specific targeting as well, but it still remains unclear how such high
348 numbers of NPs get trapped in microthrombi. One possible explanation could be that NPs get trapped
349 in forming microthrombi, *i.e.* while the clot forms, however, the large number of NPs located between
350 all components of the clot does not seem to support such a scenario. The more likely explanation is
351 that it takes some time until clots form and fully occlude a cerebral microvessel, as suggested by
352 previous investigations by us and others[20-22]. During this period, which may last for minutes or even
353 hours, vessels are not patent for cells but for plasma and since NPs travel with plasma, they enter the
354 clot and get trapped in between accumulated fibrin polymers and stalled red and white blood cells.
355 This "filtering" mechanism may explain the large number of LNDs we found in microclots and the
356 specificity with which LNDs accumulate in these structures. This concept is well in line with previous
357 studies which showed neuroprotective effects with nano-scale compounds after ischemic stroke[23, 24],
358 but did not elaborate on the mechanisms of particle distribution and cargo delivery.

359 In the current study we chose LNDs as nanocarriers because they are regarded to be non-toxic
360 and biodegradable and they have a relatively long half-life of up to 8h in mammalian blood[5]. To monitor

361 cargo release, we equipped LNDs with a FRET-based cargo release detection system, FedEcs. FRET
362 systems have been widely used in nanoscience for more than a decade[25], however, the novelty of our
363 current approach was to use a FRET pair compatible with 2-photon excitation for intravital imaging of
364 cargo release. This approach resulted in LNDs with such a high FRET signal that LNDs could be visualized
365 by 2-PM in mouse blood and brain *in vivo* in single capillary resolution. In comparison to recent, more
366 traditional approaches to image drug delivery to the brain using fluorescent NPs[12, 26, 27], FedEcs has the
367 large advantage of being able to visualize the actual moment when LNDs decompose and release their
368 cargo, even in the small number of LNDs that cross the BBB. Thus, FedEcs are able to clearly distinguish
369 between artefactual cargo delivery to the brain, that is when dyes leaked from circulating nanocarriers
370 cross the BBB, from factual cargo delivery, when carrier cross the BBB and release their cargo
371 thereafter. Thus, FedEcs will allow researchers to monitor the release of cargo from individual NPs with
372 high spatial and temporal resolution in all organs accessible to *in vivo* microscopy thereby avoiding all
373 ambiguities caused by previous methods.
374
375 **Conclusion**
376 In conclusion, we successfully developed highly fluorescent lipid nanodroplets carrying a FRET-
377 based cargo delivery system (FedEcs). FedEcs-LNDs are bright enough to be visualized in blood and
378 brain of living mice by 2-photon microscopy. Using FedEcs-LNDs we were able to quantify the stability
379 of LNDs in blood and demonstrate the preferential accumulation of LNDs in microvascular clots,
380 extravasation of intact LNDs across the blood-brain barrier, and cargo delivery to the brain parenchyma
381 following cerebral ischemia produced in controlled manner by magnetic nanoparticles. These findings
382 highlight FedEcs as a reliable and potent dynamic indicator of cargo delivery and release and provide
383 a future testing ground for the efficacy and delivery of a wide-range of targeted nanoscale therapy in
384 future.
385
386 **Acknowledgements:** The authors thank Georg Kislinger and Hanyi Jiang for the segmentation
387 and rendering of the 3D EM model and Platin Ramadani for rendering. This work was supported by the
388 European Union Horizon 2020 research and innovation program under the Marie Skłodowska-Curie
389 grant agreement No 794094, the European Research Council ERC Consolidator grant BrightSens
390 648528, the Agence National de Recherche JC/JC grant "Supertrack" ANR-16-CE09-0007, funded by
391 the Deutsche Forschungsgemeinschaft (DFG, German Research Foundation) – projects number:
392 457586042, FOR2879; A03 – Mi 694/9-1 – 428663564; DFG under Germany's Excellence Strategy
393 within the framework of the Munich Cluster for Systems Neurology (EXC 2145 SyNergy—ID
394 390857198) and the TRR 274/1 2020 – 408885537 (projects B03, C02, Z01).
395
396 **Authors contribution**

I.K. initiated and co-fund the study, led scientific aspects of the project, designed, performed and analysed most of experiments, wrote the first draft of the manuscript. N.A. formulated and optimised FRET-LNDs for 2-photon imaging. M.S. coordinated and performed CLEM experiment, helped write the manuscript. A.W. performed and designed *ex vivo* part of Nano-stroke experiment and its analyses, helped write the manuscript. V.B.T. formulated FRET-LNDs and performed their analyses. U.M. performed fMCAo stroke experiment. J.S. performed Nano-stroke and fMCAo experiments and analysis. T.M. led EM part of the project, coordinated CLEM experiments and analysis. SF designed, coordinated, performed Nano-stroke and CLEM experiments. A.K. led FRET-LNDs aspect of the project, provided infrastructure, supervised and cowrote final draft of the manuscript. N.P. led main animal experimental aspects of the project, co-fund the study, provided infrastructure, supervised, cowrote the final manuscript. All authors critically reviewed, contributed to and approved the final manuscript.

410 **Material and Methods**

411 **1. Formulation of LNDs**

412 Dye loaded nanoemulsions were obtained by spontaneous nanoemulsification. Briefly, the dyes
413 R18-TPB (prepared as described before)[28] was dissolved in LabrafacWL® at 2% by weight. In case of
414 FRET-LNDs, F888 (FRET donor, prepared as described before[5, 7]) and DiI-TPB (FRET acceptor, prepared
415 as described before[8]) Then, 60 mg of the oil with the dye were mixed with 40 mg Cremophor ELP® (also
416 called Kolliphor ELP®) and homogenized under magnetic stirring at 40 °C for 10 min. The LNDs were
417 obtained by the addition of ultrapure (Milli-Q) water (230 mg) under rapid magnetic stirring. Size
418 distributions were determined by dynamic light scattering using a Malvern Zetasizer ZSP.

419 **2. Animals**

420 Male 6-8 weeks old, 18-22 g, C57Bl6/J mice from Charles River Laboratories (Sulzfeld, Bavaria,
421 Germany) were used. Mice were group-housed under pathogen-free conditions and bred in the animal
422 housing facility of the Institute of Stroke and Dementia Research (Muenchen, Germany), with food and
423 water provided ad libitum (21 ± 1°C, at 12/12 hour light/dark cycle). Animal husbandry, health
424 screens, and hygiene management checks were performed in accordance with Federation of
425 European Laboratory Animal Science Associations (FELASA) guidelines and recommendations[29].
426 All experiments were carried out in compliance with the National Guidelines for Animal Protection of
427 Germany with the approval of the regional Animal care committee of the Government of Upper
428 Bavaria, and were overseen by a veterinarian. The data were collected in accordance with the
429 ARRIVE guidelines[30].

430 **3. Stroke fMCAo**

431 Ischemic stroke animal model via filament middle-cerebral artery occlusion (fMCAo) was
432 performed as previously described[31]. Briefly, buprenorphine (0.1 mg/kg) injected animals, 30 min later
433 were anesthetized with 1.8–2% isoflurane in 50% O_2 in air by face mask under the control of rectal
434 temperature (37°C±0.1°C) with a feedback-controlled heating pad. Regional cerebral blood flow (rCBF)
435 over the territory of the middle cerebral artery (MCA) was monitored via glued onto parietal skull
436 probe using laser Doppler fluxmetry (Perimed, Stockholm, Sweden). A silicone-coated monofilament
437 (Doccol Corporation, Sharon, MA, USA) was introduced into the left common carotid artery and
438 advanced toward the Circle of Willis until a drop of rCBF more than 80% of baseline indicated occlusion
439 of the MCA. Thereafter, animals were allowed to wake up. After 60 min, animals were re-anesthetized
440 and the filament was removed to allow reperfusion. Immediately, femoral artery catheter was inserted
441 and 30 min post-reperfusion LNDs or MNPs were injected in volumes 4 or 6 µL/g per animal,
442 respectively.

443 **4. Ex vivo: confocal (fMCAo, nano-stroke), 2-photon**

444 Animals were injected via femoral catheter by 50 µl of DyLight 649 Labeled Lycopersicon
445 Esculentum (Tomato) Lectin (Vector Laboratories, Burlingame, CA, US) and 5 min later were
446 transcardially perfused with 4% PFA in deep anesthesia. Free floating coronal 80 µm sections were
447 prepared as previously described[32]. The sections were blocked and simultaneously stained with the
448 primary antibody in buffer (1% bovine serum albumin, 0.1% gelatin from cold water fish skin, 0.5%
449 Triton X-100 in 0.01 M PBS, pH 7.2–7.4) for 72h at 4°C. The following primary antibodies were used:
450 iba-1 (rabbit, Wako, #019-19741, 1:200), NeuN (guinea pig, Synaptic Systems, #266 004, 1:100), GFAP-
451 Cy3 (mouse, Sigma Aldrich, #2905, 1:200). After incubation sections were washed in PBS and incubated
452 with the following secondary antibodies: anti-rabbit coupled to Alexa-fluor 488 (goat anti-rabbit,
453 Thermo Fisher Scientific, 1:100), anti-rabbit coupled to Alexa-fluor 594 (goat anti-rabbit, Thermo Fisher
454 Scientific, #A-11012, 1:200), anti-guinea pig coupled to Alexa-fluor 647 (goat anti-guinea pig, Thermo
455 Fisher Scientific, #A-21450, 1:200) in secondary antibody buffer (0.05% Tween 20 in 0.01 M PBS, pH
456 7.2–7.4). Nuclei were stained with 4',6-Diamidin-2-phenylindol (DAPI, Invitrogen, #D1306) 1:10,000 or
457 DRAQ5 (ThermoFisher, #65-0880-92) 1:1000 in 0.01 M PBS. Imaging was performed using confocal
458 microscopy (ZEISS LSM 900, Carl Zeiss Microscopy GmbH, Jena Germany). For NeuN and iba-1
459 quantification, 40x magnification was used (objective: EC Plan-Neofluar 40x/1.30 Oil DIC M27) with an

image matrix of 512x512 pixel, a pixel scaling of 0.4 x 0.4 µm and a depth of 8 bit. Three different ROIs in the lesion from superficial to deeper levels were chosen and collected in 15 µm z-stacks with a slice distance of 1 µm. Homotypical areas were imaged on the contralateral hemisphere and used as controls. MAP2 intensity was then measured and normalized to contralateral.

4.1 Analysis of microglia coverage. Microglia coverage was manually assessed in a maximum intensity projection of iba-1 stained sections. ROIs were chosen in the center of the lesion at 250 µm depth from the cortex surface at -1mm from bregma. Homotypical ROIs were chosen on the contralesional hemisphere. 3 ROIs per section per hemisphere were chosen. For microglia coverage, manual cell counting was used. To assess microglia morphology, Sholl and fractal analysis were performed to indicate ramification, cell range and circularity using a modified protocol from Young and Morrison[33]. Z-stack images were converted to a maximum intensity projection and microglia cells were individually cut out using the polygon selection tool in ImageJ. Only cells which were entirely contained within the z-stack were selected. Images were then thresholded and binarized as well as resized to 600 x 600 pixels, keeping the original scale. Any speckles and debris around the cell were removed using the paintbrush tool. Sholl analysis was performed using ImageJ [34]. Centered on the soma, concentric circles with an increasing radius of 1 µm were drawn, the number of intersections measured at each radius.

After converting binary images to outlines, fractal analysis was performed using the FracLac plugin for ImageJ [35]. As described previously [33], the total number of pixels present in the cell image of either the filled or outlined binary image were calculated and later transformed to µm2 (pixel area = 0,208 µm2). Cell circularity was calculated as

$$\text{Circularity} = 4*\pi*\text{Area}/\text{Perimeter}^2.$$

Statistical analysis

All data is given as mean ± standard deviation (SD) if not indicated otherwise. For comparison between groups, Student t-test was used for normally distributed data and Mann-Whitney Rank Sum test for non-normally distributed data according to the result of Kolmogorov-Smirnov normality test. Measurements over time were tested between groups using One-way or Two-way ANOVA with Repeated Measurements, followed by Turkey's multiple comparisons test for normally and Sidak's multiple comparisons test for non-normally distributed data as post hoc test. Calculations were performed with Sigmaplot version 14.0 (Systat Software GmbH, Erkrath, Germany) and GraphPad Prism version 8.4.3 (GraphPad Software, San Diego, California USA).

5. Cranial window preparation.

Before use, surgical tools were sterilized in a glass-bead sterilizer (FST, Heidelberg, Germany). Mice were anesthetized by an intra-peritoneal injection of medetomidine (0.5 mg/kg), fentanyl (0.05 mg/kg), and midazolam (5 mg/kg) (MMF) (140/10 mg/kg body weight, WDT, Bayer, Leverkusen, Germany). Subsequently, mice were placed and head-fixed in a stereotactic frame (David Kopf Instruments, Tujunga, CA, USA). Throughout the experiment, body temperature was monitored and maintained by a rectal probe attached to a feedback-controlled heating pad (Harvard Apparatus, Holliston, MA, USA). Eyes were protected from drying by applying eye ointment (Bepanthen, Bayer, Leverkusen, Germany). The scalp was washed with swabs soaked with 70 % ethanol. A flap of skin covering the cranium was excised using small scissors. The periosteum was scraped away with a 15-size scalpel (Swann Morton, Owlerton Green Sheffield, UK). The prospective craniotomy location above the primary somatosensory cortex (AP: −0.9 mm and ML: +3.0 mm relative to bregma) was marked with a biopsy punch (diameter 3 mm, Integra LifeSciences, Princeton, New Jersey, USA). The exposed skull around the area of interest was covered with a thin layer of dental acrylic (iBond Self Etch, Hereaus Kulzer, Hanau, Germany) and hardened with a LED polymerization lamp (Demi Plus, Kerr, Orange, CA, USA). A dental drill (Schick Technikmaster C1, Pluradent Frankfurt am Main, Germany) was used to thin the skull around the marked area. After applying a drop of sterile phosphate buffered saline (DPBS, Gibco, Life Technologies, Carlsbad, CA, USA) on the craniotomy the detached circular

509 bone flap was removed using forceps (S&T Vessel Dilating Forceps - Angled 45°, FST, Heidelberg,
510 Germany). Subsequently, SuperGrip forceps were used to remove carefully the dura mater (S&T
511 Forceps - SuperGrip Tips, FST, Heidelberg, Germany), and the brain was rinsed with saline. A circular
512 coverslip (3 mm diameter, thickness #0, VWR International, Radnor, PA, USA) was placed onto the
513 craniotomy and glued to the skull with histoacrylic adhesive (Aesculap AG, Tuttlingen, Germany),
514 applied via dental microbrushes (0.5 mm tip diameter, Microbrush International, Grafton, WI, USA).
515 The exposed skull was covered with dental acrylic (Tetric Evoflow A1 Fill, Ivoclar Vivadent, Schaan,
516 Liechtenstein) and a custom-made head-post was attached parallel to the window for head-fixing mice
517 in subsequent imaging sessions. After surgery, the anesthesia was antagonized with a combination of
518 Atipamezol (2.5 mg/kg), Flumazenil (0.5 mg/kg) and Naloxon (1.2 mg/kg) i.p.. Finally, mice received a
519 subcutaneous dose of the analgesic Carprophen (7.5 mg/kg body weight, Rimadyl, Pfizer, New York,
520 NY, USA) and were allowed to recover from surgery in a heating chamber.

521 **6. Intravital 2-photon**

522 2-photon images were scanned as previously described[36]. Briefly, the anesthetized mouse was
523 placed under an upright Zeiss LSM710 microscope equipped with a fs-laser (Mai Tai DeepSee, Spectra-
524 Physics, Stahnsdorf, Germany), a 20x water immersion objective (W Plan-Apochromat 20x/1.0 NA,
525 Zeiss) and a motorized stage. Ti:Sa laser (Chameleon Vision II) from 917 Coherent (Glasgow, Scotland)
526 with an excitation wavelength of 830 nm and power of 5-22 % was used for detection. GAASP detector
527 with an SP < 485 nm filter with master gain 600 for the donor channel and LP > 570 nm for the LNDs
528 acceptor or FRET channel with master gain 600 were used. Images were taken as z-stacks (150 µm,
529 1024 x 1024, 8 bit, objective: W Plan-Apochromat 20x/1.0 DIC D=0.17 M27 75mm).

530 **7. FRET in vivo**

531 There were three types of LNDs which were used at FRET in vivo experiment: loaded with donor
532 (F888), loaded with acceptor (Cy3) and with both donor and acceptor (FRET). All solutions were
533 injected in volume 7.5 µl/kg body weight into the mice with implanted cranial windows. Mouse
534 under MMF anesthesia were placed on the 2-PM stage. The LNDs were excited at 830 nm (and
535 740 nm for LNDs loaded with acceptor) and the emission was collected with SP < 485 nm (donor
536 channel) and LP > 570 (acceptor/FRET channel) filters by non-descanned detectors (photomultiplier
537 tube GaAsP, Zeiss). Three-dimensional z-stacks of 150 µm depth with 1 µm axial resolution and
538 1024×1024 pixels per image frame (0.6 µm/pixel) were acquired in multiphoton mode of the
539 microscope over a time course of 120 min. The intensity was calculated at each channel as a total
540 intensity of maximum intensity projection image using Fiji software. The FRET ratio was calculated
541 using formula: FRETratio=FRET intensity/Donor intensity. Ratiometric analysis of LNDs integrity was
542 performed in blood circulation 30-nm vs. 80-nm. Statistical analysis was performed using two-way
543 ANOVA with Tukey correction for multiple comparison (n=3 for each group) with GraphPad® Prism
544 (GraphPad Software, San Diego, CA, USA).

545 **8. Nano-stroke, a transient mini-stroke mouse model**

546 Stroke induction started one day after cranial window implantation. Throughout the experimental
547 procedure, mice were anaesthetized with an intra-peritoneal injection of medetomidine (0.5 mg/kg),
548 fentanyl (0.05 mg/kg), and midazolam (5 mg/kg) (MMF) (140/10 mg/kg) and placed on a heating pad
549 to keep body temperature at 37 °C (Harvard Apparatus, Holliston, MA, USA). The head-holder of the
550 mouse was fixed to a custom-made headpost and a neodymium-iron-boron (NdFeB) magnet was
551 placed on the cranial window overlying the distal branches middle cerebral artery (MCA; Fig. S1B, i, ii).
552 NdFeB magnets were custom-made (Zhenli Co. Ltd, Jiaozuo, Henan, China) with the following
553 specifications: Cylindrical NdFeB magnets, grade N52, 1 mm long, 1.5 mm in diameter, magnetized
554 along the cylindrical axis. Before injection, all solutions with nanoparticles were mixed thoroughly
555 using a vortex shaker (VTX-3000L, LMS). Magnetic nanoparticles, Nanomag®-D (Micromod, Rostok,
556 Germany), diameter 180 nm, PEG 2000 coated, were injected slowly at a volume of 6 µl/g body weight
557 via a femoral artery catheter. Since iron oxide is a magnetite and each particle acts as an individual
558 magnetic domain[37], we expected to block the vessels via interaction between a magnet and blood-

559 circulated MNPs. Safety, biocompatibility, and physical parameters of these MNPs were described
560 previously[10]. Subsequently, injected MNPs (Fig. S1B, ii) into the blood stream were trapped in the
561 magnetic field applied to the cerebral cortex, thereby occluding the underlying vessels as evidenced
562 by the black colour filling the vessel lumen (Fig. S1B, iii). Reperfusion was then induced by removing
563 the magnet. Ten minutes thereafter, the blood flow in the distal branches of middle cerebral artery
564 (black arrow) as well as in most pial veins was restored (Fig. S1B, iv). Vessel occlusion was monitored
565 and recorded under a stereo microscope M80 (Leica, Wetzlar, Germany), equipped with a video
566 camera DFC 290 HP (Leica). After 1 hour the magnet was removed to induce reperfusion and a
567 suspension of ultrabright FRET LNDs (7.5 µl/kg body weight) or Hypoxyprobe (60 mg/kg, NPI Inc.,
568 Edmonds, WA, USA) was injected. Systemic injection of fluorescent LNDs (Fig. S1A, i) was performed
569 through same catheter used for MNPs. The platform used for performing the nano-stroke featured a
570 custom heating pad and head-holder, which were compatible with the 2-PM stage. This allowed for
571 easy relocation of the mouse to the microscope, enabling immediate intravital imaging of the
572 reperfused area. Subsequently, mice were transferred under LSM 7 MP microscope (Zeiss,
573 Oberkochen, Germany). LNDs were excited with 830 nm wavelength, laser power 5-11%, filters, as was
574 described above, were SP < 485 nm and LP > 570 nm for donor and FRET respectively. Three-
575 dimensional z-stacks of 150 µm depth with 1 µm axial resolution and 1024×1024 pixels per image
576 frame (0.6 µm/pixel) were acquired in multiphoton mode of the microscope every 20 min over a time
577 course of 60 min. Throughout the imaging session laser power was kept below 50 mW to avoid
578 phototoxicity. Sham-operated animals received MNPs 20 min before imaging without magnet
579 application. The microthrombi were identified visually as occluded vessels (lower-to-dark fluorescent
580 intensity) or accumulated LNDs (higher fluorescent intensity). The total number of
581

582 **9. Correlated light and ATUM Volume Scanning Electron Microscopy (CLEM).**

583 In order to provide exact relocation of ROI from 2-PM to EM, the custom-made head post for head-
584 fixation was used (Figure S05, A, white arrow), as described[38]. This enabled to relocate the imaging
585 orientation from 2-PM to EM. Immediately after 2-photon imaging, mice were transcardially perfused
586 with a mixture of 4% formaldehyde and 2.5% glutaraldehyde (Electron Microscopy Sciences, EMS) in
587 0.1 M sodium cacodylate buffer, pH 7.4. After 1 h perfusion mice were decapitated and the right
588 parietal bone with the ipsilateral window was removed. Subsequently, the mouse head was attached
589 to the stage of a vibratome (VT1000S, Leica Biosystems) via the head post to cut the brain tissue with
590 thickness 80 µm parallel to the imaging plane (Figure S05A). This way, a single brain slice containing all
591 cortical layers and the complete somato-sensory cortex was obtained. The cortical brain slice was
592 incubated in the same fixative overnight at 4 °C, washed with PBS at the next day, cut at 50 µm
593 thickness on a vibratome and subsequently stored in 0.1 M sodium cacodylate buffer at 4°C until the
594 start of the postembedding. Coarse lateral relocation of the cortical region of interest was guided by
595 magnetic nanoparticles inspected under a standard binocular (Kern) and dissected at roughly 2x2 mm.
596 A standard rOTO *en bloc* staining protocol[39] was applied including postfixation in 2% osmium tetroxide
597 (EMS), 1.5% potassium ferricyanide (Sigma) in 0.1 M sodium cacodylate (Science Services) buffer (pH
598 7.4). Staining was enhanced by reaction with 1% thiocarbohydrazide (Sigma) for 45 min at 40°C. The
599 tissue was washed and incubated in 2% aqueous osmium tetroxide, washed and further contrasted by
600 overnight incubation in 1% aqueous uranyl acetate at 4°C and for 2h at 50°C. Samples were dehydrated
601 in an ascending ethanol series and infiltrated with epon-araldite resin (LX112, LADD).
602 In order to preserve the same imaging orientation for EM from the 2-photon experiment, the block
603 was trimmed parallel to the cortical surface. The advantage of MNPs is to be seen label-free in light,
604 fluorescent and electron microscopies[37]. Thereby, the correlation strategy relied on electron-dense
605 magnetic particles and further anatomical landmarks like vascular patterns (Figure S05, B) and regions
606 of MNP leftovers in the reperfused area, far outside of the ROI. The area of interest was exposed by
607 trimming using TRIM90 (Diatome) on the ATUMtome (Powertome, RMC). In total, 1500 serial sections
608 were collected starting from the pial surface with a 35° ultra-maxi diamond knife (Diatome) at a
609 nominal cutting thickness and resulting axial resolution of 100 nm and collected on freshly plasma-
610 treated (custom-built, based on Pelco easiGlow, adopted from M. Terasaki, U. Connecticut, CT), carbon

nanotube (CNT) tape (Science Services). CNT tape stripes were assembled onto adhesive carbon tape (Science Services) attached to 4-inch silicon wafers (Siegert Wafer) and grounded by adhesive carbon tape strips (Science Services). EM micrographs were acquired on a Crossbeam Gemini 340 SEM (Zeiss) with a four-quadrant backscatter detector at 8 kV. In ATLAS5 Array Tomography (Fibics), wafer overview images were generated (2000 nm/pixel). In order to relocate the region imaged by light microscopy we acquired a data set covering 10 wafers (~200 sections, covering 20 µm depth of tissue each) at a resolution of 0.2x0.2x4 µm. This coarse EM map was aligned (TrakEM2)[40] and different cell types segmented (VAST)[41]. Building on this cellular map regions of interest surrounded but devoid of magnetic particle accumulations were selected for high resolution imaging at 20x20x100 nm voxel size. High resolution stacks were aligned, segmented and rendered (Blender)[42]. Accordingly, the first step was to identify the 2-PM field-of-view on a macro photograph of the cranial window (Figure S05, C, white arrows). This ROI was identified in low resolution EM using MNPs as fiducials and vascular patterns as endogenous landmarks (Figure S05, C, black arrows). Registration of the 2-PM and the low resolution SEM image volumes allowed us to target time-lapse features of interest like microthrombi formation or extravasation events (Figure S05, D, blue arrows) and acquire high-resolution volume SEM data thereof.

References:

1. Klymchenko, A.S., Liu, F., Collot, M. & Anton, N. Dye-Loaded Nanoemulsions: Biomimetic Fluorescent Nanocarriers for Bioimaging and Nanomedicine. *Advanced Healthcare Materials* **10**, 2001289 (2021).
2. McClements, D.J. Nanoemulsions versus microemulsions: terminology, differences, and similarities. *Soft Matter* **8**, 1719-1729 (2012).
3. Kumar, M., Bishnoi, R.S., Shukla, A.K. & Jain, C.P. Techniques for Formulation of Nanoemulsion Drug Delivery System: A Review. *Prev Nutr Food Sci* **24**, 225-234 (2019).
4. Anton, N. & Vandamme, T.F. The universality of low-energy nano-emulsification. *Int J Pharm* **377**, 142-147 (2009).
5. Bouchaala, R. et al. Integrity of lipid nanocarriers in bloodstream and tumor quantified by near-infrared ratiometric FRET imaging in living mice. *Journal of Controlled Release* **236**, 57-67 (2016).
6. Anton, N. & Vandamme, T.F. Nano-emulsions and Micro-emulsions: Clarifications of the Critical Differences. *Pharmaceutical Research* **28**, 978-985 (2011).
7. Klymchenko, A.S. et al. Highly lipophilic fluorescent dyes in nano-emulsions: towards bright non-leaking nano-droplets. *RSC Adv* **2**, 11876-11886 (2012).
8. Kilin, V.N. et al. Counterion-enhanced cyanine dye loading into lipid nano-droplets for single-particle tracking in zebrafish. *Biomaterials* **35**, 4950-4957 (2014).
9. Khalin, I. et al. Size-Selective Transfer of Lipid Nanoparticle-Based Drug Carriers Across the Blood Brain Barrier Via Vascular Occlusions Following Traumatic Brain Injury. *Small* **18**, e2200302 (2022).
10. Jia, J.M. et al. Control of cerebral ischemia with magnetic nanoparticles. *Nature methods* **14**, 160-166 (2017).
11. Manzari, M.T. et al. Targeted drug delivery strategies for precision medicines. *Nature Reviews Materials* **6**, 351-370 (2021).
12. Al-Ahmady, Z.S. et al. Selective Liposomal Transport through Blood Brain Barrier Disruption in Ischemic Stroke Reveals Two Distinct Therapeutic Opportunities. *ACS Nano* **13**, 12470-12486 (2019).

661 13. Fukuta, T. et al. Neuroprotection against cerebral ischemia/reperfusion injury by intravenous
662 administration of liposomal fasudil. *International Journal of Pharmaceutics* **506**, 129-137
663 (2016).
664 14. Ishii, T. et al. Treatment of cerebral ischemia-reperfusion injury with PEGylated liposomes
665 encapsulating FK506. *Faseb j* **27**, 1362-1370 (2013).
666 15. Powers, W.J. et al. Guidelines for the Early Management of Patients With Acute Ischemic
667 Stroke: 2019 Update to the 2018 Guidelines for the Early Management of Acute Ischemic
668 Stroke: A Guideline for Healthcare Professionals From the American Heart
669 Association/American Stroke Association. *Stroke* **50**, e344-e418 (2019).
670 16. Zhou, Y. et al. Reperfusion Injury Is Associated With Poor Outcome in Patients With
671 Recanalization After Thrombectomy. *Stroke* **54**, 96-104 (2023).
672 17. Zhang, W. et al. Antithrombotic Therapy by Regulating the ROS-Mediated Thrombosis
673 Microenvironment and Specific Nonpharmaceutical Thrombolysis Using Prussian Blue
674 Nanodroplets. *Small (Weinheim an der Bergstrasse, Germany)* **18**, 2106252 (2022).
675 18. Li, S. et al. Biomimetic Nanoplatelets to Target Delivery Hirudin for Site-Specific
676 Photothermal/Photodynamic Thrombolysis and Preventing Venous Thrombus Formation.
677 *Small (Weinheim an der Bergstrasse, Germany)* **n/a**, 2203184.
678 19. Alonso-Alonso, M.L. et al. Fibrin-Targeted Nanoparticles for Finding, Visualizing and
679 Characterizing Blood Clots in Acute Ischemic Stroke. *Pharmaceutics* **14** (2022).
680 20. del Zoppo, G.J. Virchow's triad: the vascular basis of cerebral injury. *Rev Neurol Dis* **5 Suppl 1**,
681 S12-21 (2008).
682 21. Yemisci, M. et al. Pericyte contraction induced by oxidative-nitrative stress impairs capillary
683 reflow despite successful opening of an occluded cerebral artery. *Nature Medicine* **15**, 1031-
684 1037 (2009).
685 22. Schwarzmaier, S.M. et al. The Formation of Microthrombi in Parenchymal Microvessels after
686 Traumatic Brain Injury Is Independent of Coagulation Factor XI. *J Neurotrauma* **33**, 1634-1644
687 (2016).
688 23. Jiang, Y., Brynskikh, A.M., D, S.M. & Kabanov, A.V. SOD1 nanozyme salvages ischemic brain by
689 locally protecting cerebral vasculature. *J Control Release* **213**, 36-44 (2015).
690 24. Lu, Y. et al. Microthrombus-Targeting Micelles for Neurovascular Remodeling and Enhanced
691 Microcirculatory Perfusion in Acute Ischemic Stroke. *Adv Mater* **31**, e1808361 (2019).
692 25. Yang, G., Liu, Y., Teng, J. & Zhao, C.-X. FRET Ratiometric Nanoprobes for Nanoparticle
693 Monitoring. *Biosensors* **11**, 505 (2021).
694 26. Kucharz, K. et al. Post-capillary venules are the key locus for transcytosis-mediated brain
695 delivery of therapeutic nanoparticles. *Nat Commun* **12**, 4121 (2021).
696 27. Li, W. et al. BBB pathophysiology-independent delivery of siRNA in traumatic brain injury. *Sci*
697 *Adv* **7** (2021).
698 28. Reisch, A. et al. Collective fluorescence switching of counterion-assembled dyes in polymer
699 nanoparticles. *Nat Commun* **5**, 4089 (2014).
700 29. Guillen, J. FELASA guidelines and recommendations. *J Am Assoc Lab Anim Sci* **51**, 311-321
701 (2012).
702 30. Kilkenny, C., Browne, W.J., Cuthill, I.C., Emerson, M. & Altman, D.G. Improving bioscience
703 research reporting: the ARRIVE guidelines for reporting animal research. *PLoS Biol* **8**, e1000412
704 (2010).
705 31. Sienel, R.I., Kataoka, H., Kim, S.W., Seker, F.B. & Plesnila, N. Adhesion of Leukocytes to Cerebral
706 Venules Precedes Neuronal Cell Death and Is Sufficient to Trigger Tissue Damage After
707 Cerebral Ischemia. *Front Neurol* **12**, 807658 (2021).
708 32. Ghosh, M. et al. Pericytes are involved in the pathogenesis of cerebral autosomal dominant
709 arteriopathy with subcortical infarcts and leukoencephalopathy. *Ann Neurol* **78**, 887-900
710 (2015).
711 33. Young, K. & Morrison, H. Quantifying Microglia Morphology from Photomicrographs of
712 Immunohistochemistry Prepared Tissue Using ImageJ. *J Vis Exp* (2018).

34. Ferreira, T.A. et al. Neuronal morphometry directly from bitmap images. *Nature methods* **11**, 982-984 (2014).
35. Karperien, A. FracLac for ImageJ. (1999-2013).
36. Khalin, I. et al. Ultrabright Fluorescent Polymeric Nanoparticles with a Stealth Pluronic Shell for Live Tracking in the Mouse Brain. *ACS Nano* **14**, 9755-9770 (2020).
37. Reynders, H. et al. Label-Free Iron Oxide Nanoparticles as Multimodal Contrast Agents in Cells Using Multi-Photon and Magnetic Resonance Imaging. *Int J Nanomedicine* **16**, 8375-8389 (2021).
38. Luckner, M. et al. Label-free 3D-CLEM Using Endogenous Tissue Landmarks. *iScience* **6**, 92-101 (2018).
39. Kislinger, G. et al. ATUM-FIB microscopy for targeting and multiscale imaging of rare events in mouse cortex. *STAR Protocols* **1**, 100232 (2020).
40. Schindelin, J. et al. Fiji: an open-source platform for biological-image analysis. *Nature methods* **9**, 676-682 (2012).
41. Berger, D.R., Seung, H.S. & Lichtman, J.W. VAST (Volume Annotation and Segmentation Tool): Efficient Manual and Semi-Automatic Labeling of Large 3D Image Stacks. *Front Neural Circuits* **12**, 88 (2018).
42. Brito, A. Blender Quick Start Guide: 3D Modeling, Animation, and Render with Eevee in Blender 2.8. (Packt Publishing, 2018).